Interfacial toughening with self-assembled monolayers enhances perovskite solar cell reliability

Authors: Zhenghong Dai, Srinivas K. Yadavalli, Min Chen, Ali Abbaspourtamijani, Yue Qi, Nitin P. Padture*

Affiliation: School of Engineering, Brown University, Providence, RI 02912, USA

*Correspondence to: nitin_padture@brown.edu

Abstract:

Iodine-terminated self-assembled monolayer (I-SAM) was used in perovskite solar cells (PSCs) to achieve a 50% increase of adhesion toughness at the interface between the electron transport layer (ETL) and the halide perovskite thin film to enhance mechanical reliability. Treatment with I-SAM also improved the power conversion efficiency from 20.2% to 21.4%, reduced hysteresis, and improved operational stability with a projected T80 (80% of the initial efficiency retained) increasing from ~700 hours to 4,000 hours at 1-sun and with continuous maximum-power-point tracking. Operational-stability-tested PSC without SAMs revealed extensive irreversible morphological degradation at the ETL-perovskite interface, including voids formation and delamination, whereas PSCs with I-SAM exhibited minimal damage accumulation. This difference was attributed to a combination of a decrease in hydroxyl groups at the interface and the higher interfacial toughness.

One Sentence Summary: Self-assembled monolayers enhance simultaneously interfacial toughness, performance, operational stability, and reliability of perovskite solar cells.

Main Text:

The promise of low cost, high power conversion efficiency (PCE,) and versatility has driven research efforts on perovskite solar cells (PSCs) (*1-3*). The low formation energies of metal-halide perovskites (MHPs) light absorbers that enable solution-processing at or near room temperature (*4*) also makes them unstable (*5, 6*). Research on improving PSC operational stability (*5, 6*) has made steady progress, but PSCs will also need to be mechanically reliable if they are to operate efficiently for decades (*6, 8-11*). Enhancing the mechanical reliability of PSCs is particularly challenging because the low formation energies of MHPs result in inherently poor mechanical properties, in that they are compliant (low Young's modulus, E), soft (low hardness, H), and brittle (low toughness, G_C) (*9*). For example, the prototypical MHP, methylammonium lead triiodide ($CH_3NH_3PbI_3$ or $MAPbI_3$), has E~17.8 GPa, H~0.6 GPa, and G_C~2.7 $J.m^{-2}$ (cohesion) as measured by nanoindentation of single-crystals (*9*). Furthermore, interfaces between the MHP thin film and the adjacent functional layers in planar PSCs multilayer stack are even more brittle, with G_C<1.5 $J.m^{-2}$ (adhesion) (*8, 10, 12, 13*), making them prone to premature delamination.

The sources of internal and external mechanical stresses in PSCs that can drive fracture include (*9, 11*): (i) coefficient of thermal expansion (CTE) mismatch between the layers; (ii) in-service thermal excursions; (iii) in-service damage-accumulation; and (iv) deformation during manufacturing, installation, maintenance, and service (such as bending, stretching, and twisting). In tandem PVs incorporating PSCs the CTE-induced internal stresses are expected to be even higher due to the additional layers, and in the case of flexible single-junction PSCs, the externally applied stresses are typically more severe (*9, 11*). Although the ultimate in-service delamination failure of devices depends on many factors, G_C of the weakest interface — akin to the weakest link

in a chain — is perhaps the most important metric that determines the mechanical reliability of multilayer devices (*14*).

There have been a few attempts to enhance the G_C of the weakest interface in PSCs, with varying degrees of success, using approaches such as adding interfacial layers (*10, 15-18*), scaffolding (*19*), interpenetrating interfaces (*20*), introducing additives (*13, 21*), and grain coarsening (*12*). Here we demonstrate the substantial toughening of the brittle interface between the MHP thin film and the underlying SnO_2 electron-transport layer (ETL) using an iodine-terminated self-assembled monolayer (I-SAM) that acts as a "molecular glue." This processing step not only increased PCE (up to 21.44%) and reduced hysteresis but also improved operational stability under 1-sun maximum-power-point (MPP) continuous operation (projected T80, time to 80% PCE retention, up to ~4,000 h). The characterization of the operational-stability-tested PSCs reveals that the I-SAM helped preserve the mechanical integrity of the ETL/MHP interface, and what is termed as "operational stability" in previous PSC studies is closely intertwined with mechanical reliability. We note that SAMs have been used to toughen interfaces in other types of devices while improving other functional properties, e.g. thermal conductivity (*22*).

We chose the mixed-composition MHP, $Cs_{0.05}(FA_{0.85}MA_{0.15})_{0.95}Pb(I_{0.85}Br_{0.15})_3$ with 4 mol% excess PbI_2 (FA=formamidinium or $HC(NH_2)_2^+$), optimized for high PCE and stability (*23*) and SnO_2 as the ETL, as it provides a more favorable energy-level alignment with this MHP and minimizes the photocatalytic degradation of the MHP compared to TiO_2. The 3-iodopropyl trimethoxysilane ($Si(OCH_3)_3(CH_2)_3I$) I-SAM, with —$Si(OCH_3)_3$ anchor group, —I terminal group, and alkyl $(CH_2)_n$ chain (n=3) linker, is chosen based on the following considerations. First, the surface of SnO_2 ETL, as with most oxides (*24*), is covered with adsorbed hydroxyl (—OH) groups that get trapped during deposition of the MHP thin film on top in *n-i-p* "regular" planar

PSCs, and degrade performance (*25, 26*). Trialkoxysilane SAMs are known to self-assemble and cross-link readily on such oxide surfaces by the silanization process (*27*) and greatly reduce the number of surface —OH groups as they create anchoring —O-Si bonds. Second, assuming a "brush-like" SAMs morphology due to the short alkyl chain length used here, the —I terminal group is expected to form electrostatic bonds to the MHP thin film on top (*28*). A control H-SAM with —H terminal group ($Si(OCH_3)_3(CH_2)_3H$) was used in separate experiments to isolate the effects of the —I terminal group. Third, the short length of the alkyl chain (n=3) makes the SAMs-coated surface sufficiently lyophilic for the subsequent solution-deposition of the MHP thin film. Finally, SAMs in general (*29, 30*), and trialkoxysilane-based SAMs in particular (*31, 32*), increase PCE and reduce hysteresis in PSCs through improved extraction of photocarriers, reduced charge accumulation at interfaces, and passivation of interfacial charge traps.

We measured the adhesion toughness, G_C, of the ETL/MHP interface using the "sandwich" double-cantilever beam (DCB) delamination method (Fig. 1A) (*8, 10, 12, 14*), as described in Supplementary Materials (SM) and fig. S1. The SnO_2 ETL was deposited on indium-tin-oxide (ITO) coated glass substrates using the method of Jiang, *et al*. (*33*). The SAM was deposited on the SnO_2 surface by dip-coating at room temperature using the procedure described in the SM. We note that SAMs deposition is sensitive to several experimental parameters such as water content, solvent used, solution age, deposition time, temperature, etc. (*27*). The presence of Si on the H-SAM-coated ETL surface, and both Si and I on the I-SAM-coated ETL surface, was confirmed with X-ray photoelectron spectroscopy (XPS, fig. S2). The MHP thin film (~500-nm thickness) was then deposited through a variation of the solvent-engineering method (*34*). X-ray diffraction (XRD) patterns of the MHP thin films without SAMs, and ones with H-SAM or I-SAM underneath (fig. S3) showed no difference in the thin-film MHP phase. Similarly, the top-surface scanning

electron microscope (SEM) images in figs. S4, A to C, showed no discernable difference in the MHP thin-film microstructure: the average apparent grain sizes of the MHP thin films are between ~330 to ~370 nm.

The G_C of the ETL/MHP interface (Fig. 1B and table S1) was enhanced by ~50% with I-SAM (1.91±0.48 J.m^{-2} to 2.83±0.35 J.m^{-2}). For H-SAM, the mechanical bonding with MHP was weak, resulting in a decreased G_C to 1.72±0.54 J.m^{-2}. Delamination failure occurred at the ETL/MHP interface in each case; scanning electron microscopy (SEM) images of the mating fracture surfaces are shown in figs. S5, A to F. For I-SAM case, the SEM image of the SnO_2 ETL side fracture surface showed a few adhered smaller MHP grains due to occasional intergranular fracture.

Density functional theory (DFT) calculations were performed to study the adhesion provided by the interfacial bonding between MHP surface and idealized 'brush-like" SAMs (see SM for details) (*35-42*), where we used α-$FAPbI_3$ to represent the MHP. Aligned butane ($H(CH_2)_4H$) and I-terminated butane (($H(CH_2)_4I$) molecules were used to represent H-SAM and I-SAM, respectively, because the Si-based anchor group in the SAMs was unlikely to influence the bonding at the other end of the alkyl chains. The adhesion of α-$FAPbI_3$ (001) surfaces, of different terminations, with $H(CH_2)_4I$ was found to be about twice that with $H(CH_2)_4H$ (table S2 and fig. S6). The strongest adhesion was achieved at the PbI_2-terminated α-$FAPbI_3$ (001) surface with two aligned $H(CH_2)_4I$ molecules per unit cell (near-ideal packing density of 20 Å^2 per molecule). The interfacial bonding with I-SAM has the characteristics of the halogen bond, where a low electron-density region on a covalently-bonded halogen atom (mainly in the heavier halogens) form attractive interaction with electron-rich sites (*43*). The electrophilic regions associated with the halogen atoms on $H(CH_2)_4I$ gained electrons from both the under-coordinated Pb^{2+} (electron

donor) and fully-coordinated I^- (nucleophile) on the PbI_2-terminated α-$FAPbI_3$ (001) surface (Fig. 1D). Halogen bonding changes with electrophilic order: I > Br > Cl > F, which increases with the polarizability and decreases with the electronegativity. A similar interface using $H(CH_2)_4F$ molecules at the other extreme of the electrophilic order confirms this trend (table S2). Naturally, no such bond is expected at the interface with $H(CH_2)_4H$ (Fig. 1C). The lack of electron transfer and the longer I…H and Pb…H distances indicated the absence of chemical bonding (see results in fig. S6 and table S2 for other α-$FAPbI_3$ surface terminations and different packing densities). Although I-SAM in the experiments may not be as idealized ("brush-like", full-coverage), the DFT calculations support the hypothesis that I-termination enhances the bonding with the MHP surface substantially, and that it is preferred over other halogen terminations. The latter was further confirmed experimentally using 3-bromopropyl trimethoxysilane ($Si(OCH_3)_3(CH_2)_3Br$) Br-SAM, where an average G_C of 2.08±0.31 $J.m^{-2}$ was measured (table S1), which is in-between H-SAM and I-SAM cases.

We fabricated PSCs with planar *n-i-p* "regular" architecture (Fig. 2A), for different SAMs combinations (see SM for device fabrication and testing details). Cross-sectional SEM images in Fig. 2, B to D, showed no discernable differences. The current density (J) – voltage (V) response of the "champion" PSCs without SAMs, and ones with H-SAM or I-SAM are presented in Fig. 2E, and the corresponding PV performance parameters are listed in Table 1. The I-SAM increased V_{OC}, and both PSCs with SAMs showed lower hysteresis indices (1.8% H-SAM and 2.9% I-SAM, versus 8.8% without SAMs). The short-circuit current density (J_{SC}) values for all PSCs compared favorably with the respective values derived from the external quantum efficiency (EQE) spectra of these PSCs in Fig. 2F. The stabilized PCE output at MPP of these three PSCs is presented in fig. S7.

Statistics for the PV performance parameters J_{SC}, V_{OC}, fill factor (FF), and PCE for 20 each PCSs are presented in figs. S8, A to D, with average PCE of without SAMs 19.04±0.49%, with H-SAM 19.04±0.48%, and with I-SAM 20.20±0.62%, confirming overall increased performance of the latter, and also demonstrating reproducibility. The increased PCE in PSCs with I-SAM was largely the result of the increased V_{OC}. In this context, the estimated trap-filled-limited voltages (V_{TFL}) for electron-only transport devices shown in fig. S9 were used to estimate trap densities (n_{Trap}) of 5.21×10^{15} cm^{-3} for device without SAMs, 1.98×10^{15} cm^{-3} for the device with H-SAM, 1.36×10^{15} cm^{-3} for the device with I-SAM. We attributed the increased V_{OC} to the passivation of charge traps that improved extraction of electrons. The reduced hysteresis with both SAMs was attributed to the reduced charge accumulation with fewer surface —OH groups. Similar increases in PSC performance with different types of SAMs have been demonstrated in several studies (*25*, *28-32*).

In Fig. 3, we present the operational stability of PSCs under continuous 1-sun illumination with MPP-tracking. In all the tested PSCs, there was initial "burn-in" instability with a decline, rise, or both in PCE followed by linear steady-state degradation, as has been seen previously for single-junction PSCs (*44*). Following a method proposed by Khenkin *et al*. (*44*), we estimated T80 of PSCs without SAMs of ~692 h and with H-SAM of ~714 h (see SM for details). The steady-state degradation of these PSCs appeared to occur at about the same rate. The extrapolated T80 durations for the three PSCs with I-SAM, assuming linear degradation, were estimated at ~3,006 h, ~1,896, and ~3,921 h. The normalized PV performance parameters (J_{SC}, V_{OC}, FF, and PCE) of the PSCs from the *J-V* responses measured during operational-stability testing are presented in figs. S10, A to D. (Note that PCE derived from the *J-V* response was typically higher than that measured by MPP-tracking (*44, 45*).) The performance degradation in the PSC without SAMs was

in all three parameters J_{SC}, V_{OC}, and FF. Table S3 presents PV performance parameters of the PSCs with SAMs, before and after the completion of operational-stability testing, showing decay primarily in V_{OC} and FF.

The operational-stability-tested PSCs were characterized by cross-sectioning one half of each of these devices and deliberately delaminating the other half. Cross-sectional SEM images of the PSC without SAMs (Fig. 4, A to C) showed three types of irreversible morphological-degradation features at the interface compared with the corresponding "before" SEM image in Fig. 2B: small voids, large voids, and delamination. In PSC with H-SAM (Fig. 4D), although voids were not apparent, interfacial delamination was observed. In contrast, such degradation features were not seen in the PSC with I-SAM in the SEM image in Fig. 4E, which looked similar to the corresponding "before" SEM image in Fig. 2D.

Figure 4, F to I, are SEM images of the perovskite bottom side fracture surfaces of the same delaminated PSCs. Consistent with the cross-sectional observations, the perovskite bottom side fracture surface of the PSC without SAMs showed small voids, large voids (Fig. 4F), and delamination (Fig. 4G). Light-contrast degradation-product particles were also seen in Fig. 4, F and G, which were absent in the pristine interface (fig. S5B). In PSC with H-SAM (Fig. 4H) delamination and some voids were observed. In comparison, degradation features in the PSCs with I-SAM were relatively unremarkable (Fig. 4I), which is, once again, consistent with the corresponding cross-sectional SEM image (Fig. 4E).

We attributed the reduced severity of irreversible degradation of the ETL/MHP interface with I-SAM, and the attendant decay in the PSC performance, to the following effects of the I-SAM. First, both H-SAM and I-SAM should reduce the prevalence of —OH groups at the SnO_2 ETL surface. This reduction in positively charged point-defects (*25*) should slow down the ion-

migration-induced formation of interfacial voids that can serve as sites for photocarriers recombination (*46*) and nucleation of interfacial delamination cracks. The enhanced G_C of the ETL/MHP interface with I-SAM should impede propagation of these incipient interfacial delamination cracks that would block electric current (*46*). To isolate the effect of light, we exposed the DCB specimens without SAMs, and ones with H-SAM or I-SAM to 1-sun (LED) continuous illumination in air (~35 °C, ~40% relative humidity) from the bottom for 120 h or 240 h, and then tested them to measure the G_C. The results in fig. S11 and table S4 show that after 240-h exposure there was 14% and 17% loss in the average G_C in without SAMs and with H-SAM cases, respectively, but only 5% for the with I-SAM case. This suggested that the light-induced reduction in G_C in specimens without SAMs and ones with H-SAM, both with initial lower G_C (Fig. 1B), also contributed to the degradation of their respective PSCs.

We chose the most brittle interface (ETL/MHP) in PSCs for SAMs-induced toughening for maximum impact. When sufficiently toughened, delamination failure will shift to the next weakest interface in the PSC multilayer stack, and so on (*9, 10*), so further efforts will need to focus on toughening the other PSC interfaces using SAMs. Room-temperature solution-deposition of SAMs is a low-cost approach that is amenable to scale-up for batch and/or continuous manufacturing of a wide variety of PSCs (rigid, flexible, tandem). Eventually, when all the interfaces are sufficiently toughened and optimized, the ultimate failure of PSCs will be determined by fracture within the individual layers. Toughening of the individual layers themselves, for example by incorporating reinforcements as in ceramic or polymer nanocomposites, while simultaneously improving their functional properties, will be the next challenge.

References and Notes:

1. N.-G. Park, M. Grätzel, T. Miyasaka, *Organic-Inorganic Halide Perovskite Photovoltaics: From Fundamentals to Device Architectures*. (Springer, Zurich, Switzerland, 2016).

2. H. J. Snaith, "Present status and future prospects of perovskite photovoltaics," *Nat. Mater.* **17**, 372-376 (2018).

3. A. K. Jena, A. Kulkarni, T. Miyasaka, "Halide perovskite photovoltaics: background, status, and future prospects," *Chem. Rev.* **119**, 3026-3103 (2019).

4. W. A. Dunlop-Shohl, Y. Zhou, N. P. Padture, D. B. Mitzi, "Synthetic approaches for halide perovskite hhin films," *Chem. Rev.* **119**, 3193-3295 (2019).

5. Y. Rong, Y. Hu, A. Mei, H. Tran, M. I. Saidaminov, S. I. Seok, M. McGehee, E. H. Sargent, H. Han, "Challenges for commercializing perovskite solar cells," *Science* **361**, 1214 (2018).

6. S. P. Dunfield, L. Bliss, F. Zhang, J. M. Luther, K. Zhu, M. F. A. M. van Hest, M. O. Reese, J. J. Berry, "From Defects to Degradation: A mechanistic understanding of degradation in perovskite solar cell devices and modules," *Adv. Energy Mater.* **10**, 1904054 (2020).

7. Z. Li, T. R. Klein, D. H. Kim, M. J. Yang, J. J. Berry, M. F. A. M. van Hest, K. Zhu, "Scalable fabrication of perovskite solar cells," *Nat. Rev. Mater.* **3**, 18017 (2018).

8. N. Rolston, B. L. Watson, C. D. Bailie, M. D. McGehee, J. P. Bastos, R. Gehlhaar, J.-E. Kim, D. Vak, A. T. Mallajosyula, G. Gupta, A. D. Mohite, R. H. Dauskardt, "Mechanical integrity of solution-processed perovskite solar cells," *Extreme Mech. Lett.* **9**, 353-358 (2016).

9. C. Ramirez, S. K. Yadavalli, H. F. Garcces, Y. Zhou, N. P. Padture, "Thermo-mechanical

behavior of organic-inorganic halide perovskites for solar cells," *Scripta Mater.* **150**, 36-41 (2018).

10. N. Rolston, A.D. Printz, J.M. Tracy, H.C. Weerasinghe, D. Vak, L.J. Haur, A. Priyadarshi, N. Mathews, D.J. Slotcavage, M.D. McGehee, R.E. Kalan, K. Zielinski, R.L. Grimm, H. Tsai, W. Nie, A.D. Mohite, S. Gholipour, M. Saliba, M. Grätzel, R. H. Dauskardt, "Effect of cation composition on the mechanical stability of perovskite solar cells," *Adv. Energy Mater.* **8**, 1702116 (2018).
11. S. K. Yadavalli, Z. Dai, H. Zhou, Y. Zhou, N. P. Padture, "Facile crack-healing in organic-inorganic halide perovskite thin films," *Acta Mater.* **187**, 112-121 (2020).
12. Z. Dai, S. K. Yadavalli, M. Hu, M. Chen, Y. Zhou, N. P. Padture, "Effect of grain size on the fracture behavior of organic-inorganic halide perovskite thin films for solar cells," *Scripta Mater.* **185**, 47-50 (2020).
13. M. Gutwald, N. Rolston, A. D. Printz, O. Zhao, H. Elmaraghi, Y. Ding, J. Zhang, R. H. Dauskardt, "Perspectives on intrinsic toughening strategies and passivation of perovskite films with organic additives," *Solar Energy Mater. Solar Cells* **209**, 110433 (2020).
14. J.-H. Kim, I. Lee, T.-S. Kim, N. Rolston, B. L. Watson, R. H. Dauskardt, "Understanding mechanical behavior and reliability of organic electronic materials," *MRS Bull.* **42**, 115-123 (2017).
15. J. H. Yun, J.S. Yun, A. Ho-Baillie, S. Huang, S.H. Woo, Y. Heo, J. Seidel, F. Huang, Y.-B. Cheng, M.A. Green, "Synergistic enhancement and mechanism study of mechanical and moisture stability of perovskite solar cells introducing polyethylene-imine into the $CH_3NH_3PbI_3$/HTM interface," *J. Mater. Chem. A* **3**, 2176-2182 (2015).
16. B. L. Watson, N. Rolston, K. A. Bush, T. Leijtens, M. D. McGehee, R. H. Dauskardt, "Cross-

linkable, solvent-resistant fullerene contacts for robust and efficient perovskite solar cells with increased J_{SC} and V_{OC}," *ACS Appl. Mater. Interf.* **8**, 25896−25904 (2016).

17. S. Jeong, I. Lee, T.-S. Kim, J.-Y. Lee, "An interlocking fibrillar polymer layer for mechanical stability of perovskite solar cells," *Adv. Mater. Interf.* **7**, 20001425 (2020).

18. S. Song, E. Y. Park, B. S. Ma, D. J. Kim, H. H. Park, Y. Y. Kim, S. S. Shin, N. J. Jeon, T.-S. Kim, J. Seo, "Selective defect passivation and topographical control of 4-dimethylaminopyridine at grain boundary for efficient and stable planar perovskite solar cells," *Adv. Energy Mater.* **11**, 2003382 (2021).

19. B. L. Watson, N. Rolston, A. D. Printz, R. H. Dauskardt, "Scaffold-reinforced perovskite compound solar cells," *Energy Environ. Sci.* **10**, 2500-2508 (2017).

20. Q. Dong, C. Zhu, M. Chen, C. Jiang, J. Guo, Y. Feng, Z. Dai, S. K. Yadavalli, M. Hu, X. Cao, Y. Li, Y. Huang, Z. Liu, Y. Shi, L. Wang, N. P. Padture, Y. Zhou, "Interpenetrating interfaces for efficient perovskite solar cells with high operational stability and mechanical robustness." *Nat. Commun*. **12**, 973 (2021).

21. J. Tong, J. Gong, M. Hu, S. K. Yadavalli, Z. Dai, F. Zhang, C. Xiao, J. Hao, M. Yang, M. A. Anderson, E. L. Ratcliff, J. J. Berry, N. P. Padture, Y. Zhou, K. Zhu, "High-performance methylammonium-free ideal-band-gap perovskite solar cells," *Matter*, in press (2021). doi: 10.1016/j.matt.2021.01.003

22. P. J. O'Brien, S. Shenogin, J. Liu, P. K. Chow, D. Laurencin, P. H. Mutin, M. Yamaguchi, P. Keblinski, G. Ramanath, "Bonding-induced thermal conductance enhancement at inorganic heterointerfaces using nanomolecular monolayers," *Nat. Mater.* **12**, 118-122 (2013).

23. M. Saliba, T. Matsui, J.-Y. Seo, K. Domanski, J.-P. Correa-Baena, M. K. Nazeeruddin, S.

M. Zakeeruddin, W. Tress, A. Abate, A. Hagfeldt, M. Grätzel, "Cesium-containing triple cation perovskite solar cells: improved stability, reproducibility and high efficiency," *Energy Environ. Sci.* **9**, 1989-1997 (2016).

24. C. Noguera, *Physics and Chemistry at Oxide Surfaces*. (Cambridge University Press, Cambridge, UK, 1996).

25. G. Tumen-Ulzii, T. Matsushima, D. Klotz, M. R. Leyden, P. Wang, C. Qin, J.-W. Lee, S.-J. Lee, Y. Yang, C. Adachi, "Hysteresis-less and stable perovskite solar cells with a self-assembled monolayer," *Commun. Mater.* **1**, 31 (2020).

26. Z. Liu, L. Qiu, L. K. Ono, S. He, Z. Hu, M. Jiang, G. Tong, Z. Wu, Y. Jiang, D.-Y. Son, Y. Dang, S. Kazaoui, Y. Qi, "A holistic approach to interface stabilization for efficient perovskite solar modules with over 2,000-hour operational stability," *Nat. Energy* **5**, 596-604 (2020).

27. A. Ulman, "Formation and structure of self-assembled monolayers," *Chem. Rev*. **96**, 1533-1554 (1996).

28. A. Abate, M. Saliba, D. J. Hollman, S. D. Stranks, K. Wojciechowski, R. Avolio, G. Grancini, A. Petrozza, H. J. Snaith, "Supramolecular halogen bond passivation of organic-inorganic halide perovskite solar cells, *Nano Lett*., **14**, 3274-3254 (2014).

29. P. Schulz, D. Cahen, A. Kahn, "Halide perovskites: Is it all about the interface? " *Chem. Rev.* **119**, 3349-3417 (2019).

30. S. Y. Kim, S. J. Cho, S. E. Byeon, X. He, H. Y. Yoon, "Self-assembled monolayers as interface engineering nanomaterials in perovskite solar cells," *Adv. Energy Mater.* **10**, 2002606 (2020).

31. L. Liu, A. Mei, T. Liu, P. Jiang, Y. Sheng, L. Zhang, H. Han, "Fully printable mesoscopic

perovskite solar cells with organic silane self-assembled monolayer," *J. Am. Chem. Soc.* **137**, 1790-1793 (2015).

32. G. Yang, C. Wang, H. Lei, X. Zheng, P. Qin, L. Xiong, X. Zhao, Y. Yan, G. Fang, "Interface engineering in planar perovskite solar cells: energy level alignment, perovskite morphology control, and high performance achievement," *J. Mater. Chem. A* **5**, 1658-1666 (2017).

33. Q. Jiang, L. Zhang, W. H, X. Yang, J. Meng, H. Lu, Z. Yin, J. Wu, X. Zhang, "Enhanced electron extraction using SnO_2 for high-efficiency planar-structure $HC(NH_2)_2PbI_3$-based perovskite solar cells," *Nat. Energy* **2**, 16177 (2016).

34. N. J. Jeon, J. H. Noh, Y. C. Kim, W. S. Yang, S. Ryu, S. I. Seok, "Solvent engineering for high-performance inorganic-organic hybrid perovskite solar cells," *Nat. Mater.* **9**, 897-903 (2014).

35. G. Kresse, J. Furthmüller, "Efficiency of *ab initio* total energy calculations for metals and semiconductors using a plane-wave basis set," *Comput. Mater. Sci.* **6**, 15-50 (1996).

36. G. Kresse, J. Furthmüller, "Efficient iterative schemes for *ab initio* total-energy calculations using a plane-wave basis set," *Phys. Rev. B* **55**, 11169 (1996).

37. J. P. Perdew, K. Burke, M. Ernzerhof, "Generalized gradient approximation made simple," *Phys. Rev. Lett.* **77**, 3865 (1996).

38. S. Grimme, J. Antony, S. Ehrlich, H. Krieg, "A consistent and accurate *ab initio* parametrization of density functional dispersion correction (DFT-D) for the 94 elements H-Pu," *J. Chem. Phys.* **132**, 154104 (2010).

39. A. A. Tamijani, A. Salam, M. P. d. Lara-Castells, "Adsorption of noble-gas atoms on the TiO_2(110) surface: An *ab initio*-assisted study with van der Waals-corrected DFT," *J. Phys. Chem. C* **120**, 18126-18139 (2016).

40. M. T. Weller, O. J. Weber, J. M. Frost, A. Walsh, "Structure of black formamidinium lead iodide, α-[$HC(NH_2)_2$]PbI_3, at 298 K," *J. Phys. Chem. Lett.* **6**, 3209-3212 (2015).

41. J. Liu, J. Kang, S. Chen, J. J. White, H. Yin, P. Liu, H. Zhao, Y. Wang, "Effects of compositional engineering and surface passivation on the properties of halide perovskites: a theoretical understanding," *Phys. Chem. Chem. Phys.* **22**, 19718-19724 (2020).

42. Y. Qi, L. G. Hector, "Adhesion and adhesive transfer at aluminum/diamond interfaces: A first-principles study," *Phys. Rev. B* **69**, 235401 (2004).

43. G. Cavallo, P. Metangolo, R. Milani, T. Pilati, A. Priimagi, G. Resnati, G. Terraneo, "The halogen bond, " *Chem. Rev*. **116**, 2478-2601 (2016).

44. M. V. Khenkin, E. A. Katz, A. Abate, G. Bardizza, J. J. Berry, C. Brabec, F. Brunetti, V. Bulović, Q. Burlingame, A. D. Carlo, R. Cheacharoen, Y.-B. Cheng, A. Colsmann, S. Cros, K. Domanski, M. Dusza, C. J. Fell, S. R. Forrest, Y. Galagan, D. D. Girolamo, M. Grätzel, A. Hagfeldt, E. van Hauff, H. Hoppe, J. Kettle, H. Köbler, M. S. Leite, S. Liu, Y.-L. Loo, J. M. Luther, C.-Q. Ma, M. Madsen, M. Manceau, M. Matheron, M. McGehee, R. Meitzner, M. K. Nazeeruddin, A. F. Nogueira, Ç. Odabaşı, A. Osherov, N.-G. Park, M. O. Reese, F. D. Rossi, M. Saliba, U. S. Schubert, H. J. Snaith, S. D. Stranks, W. Tress, P. A. Troshin, V. Turkovic, S. Veenstra, I. Visoly-Fisher, A. Walsh, T. Watson, H. Xie, R. Yıldırım, S. M. Zakeeruddin, K. Zhu, M. Lira-Cantu, "Consensus statement for stability assessment and reporting for perovskite photovoltaics based on ISOS procedures," *Nat. Energy* **5**, 35-49 (2020).

45. M. Saliba, M. Stolterfoht, C. M. Wolff, D. Neher, A. Abate, "Measuring aging stability of perovskite solar cells," *Joule* **2**, 1019-1027 (2018).

46. D. Bi, X. Li, J. V. Milić, D. J. Kubicki, N. Pellet, J. Luo, T. LaGrange, P. Mettraux, L.

Emsley, S. M. Zakeeruddin, M. Grätzel, "Multifunctional molecular modulators for perovskite solar cells with over 20% efficiency and high operational stability," *Nat. Commun.* **9**, 4482 (2018).

Acknowledgments:

Experimental assistance from M. Hu, N. Pellet, and Y. Zhou is gratefully acknowledged. **Funding:** The work of Z.D., S.K.Y. M.C., and N.P.P was supported by the Office of Naval Research (grant nos. N00014-17-1-2232 and N00014-20-1-2574) and the National Science Foundation (NSF; grant no. 1538893). The work of A.A. and Y.Q. was supported by NSF Center for Synthetic Organic Electrochemistry (grant no. 2002158). **Author contributions:** N.P.P. conceived, designed, and supervised the research. Z.D., S.K.Y., and M.C. fabricated the thin films and the devices. Z.D. characterized and tested the thin films and the devices. A.A and Y.Q. performed the DFT calculations. N.P.P. and Z.D. interpreted the data and wrote the manuscript, with contributions from the other authors. **Competing interests:** Authors declare no competing interests. A patent application is being filed. **Data and materials availability:** All data are available in the main text or the supplementary materials.

Materials and Methods
Supplementary Text
Figs. S1-S11
Tables S1-S4

Main Figures:

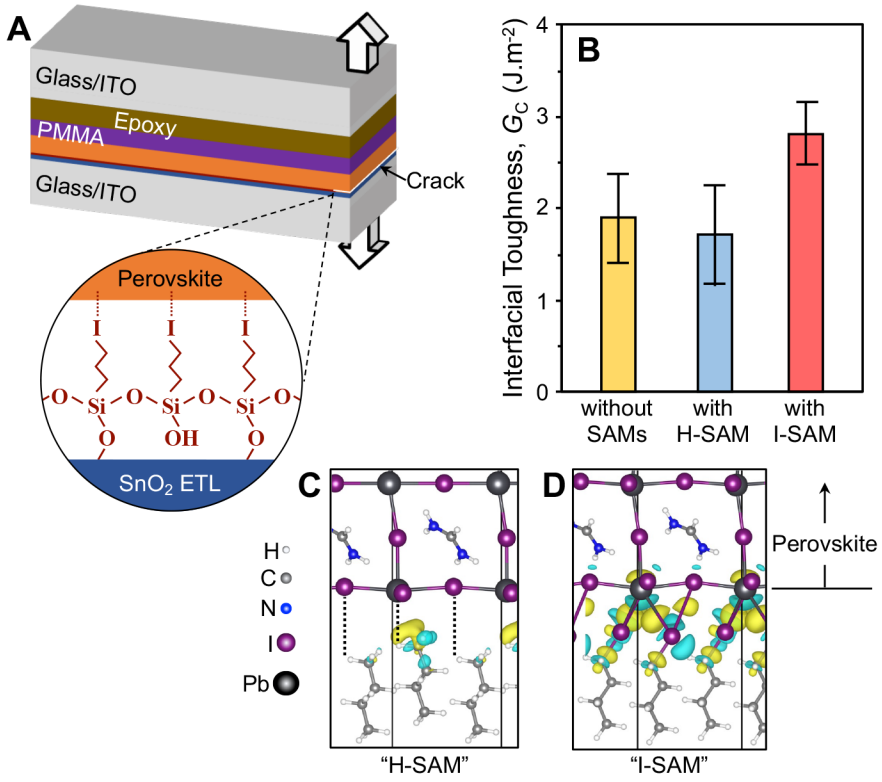

Figure 1. Mechanical behavior of the ETL/MHP interface. (A) Schematic illustration of the "sandwich" DCB specimen for toughness testing (not to scale). Inset: magnified schematic illustration of idealized I-SAM. (B) Toughness of ETL/MHP interface without SAMs, and ones with H-SAM or I-SAM. The histograms and error bars represent average and standard deviation, respectively, of 12 specimens each (see table S1 for the data). Charge-transfer-density difference plots from DFT calculations. Bonding between PbI_2-terminated α-$FAPbI_3$ (001) surface and: (C) $H(CH_2)_3H$ ("H-SAM") or (D) $H(CH_2)_3I$ ("I-SAM"). The yellow or blue colors indicate electron gain or loss above 0.0007 $e.Å^{-3}$, respectively. Dashed lines across the interface indicate no bonding.

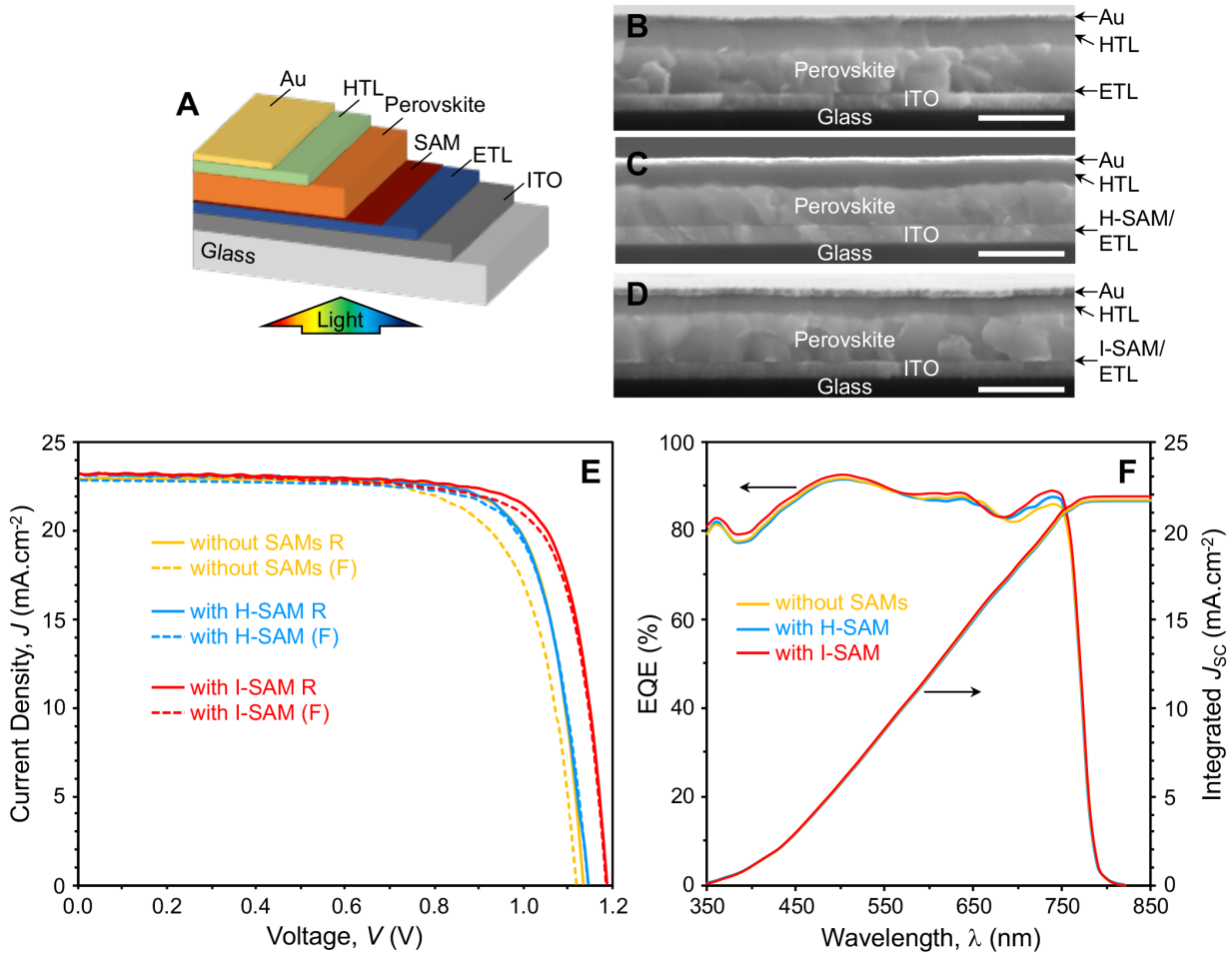

Figure 2. Structure and performance of PSCs. (A) Schematic illustration (not to scale) of the *n-i-p* "regular" planar PSCs with SAMs (SAMs absent in control PSC). Cross-sectional SEM images of as-fabricated PSCs (scale bar = 1 μm): (B) without SAMs, (C) with H-SAM, and (D) with I-SAM. (E) *J-V* responses, in reverse (R) and forward (F) scans, of "champion" PSCs without SAMs, and ones with H-SAM or I-SAM. (See Table 1 for PV performance parameters.) (F) EQE spectra and integrated J_{SC} of the "champion" PSCs without SAMs, and ones with H-SAM or I-SAM.

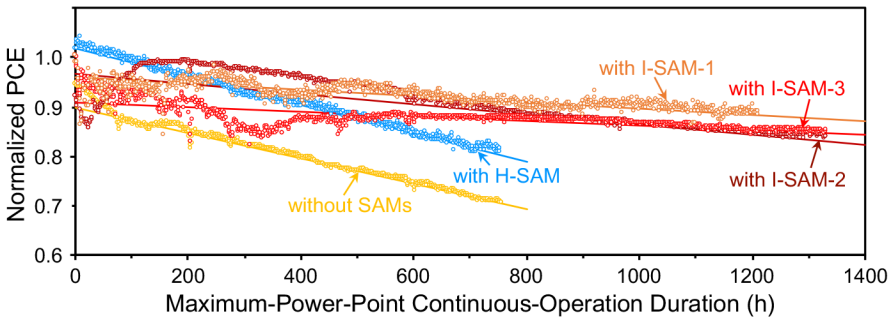

Figure 3. Normalized PCE of PSCs with SAMs, and ones with H-SAM or I-SAM (three devices) as a function of time under the following conditions: 1-sun continuous illumination, MPP-tracking, unencapsulated, flowing N_2 atmosphere, and room-temperature. PCE recorded approximately every hour. The lines are linear fits to the data after initial "burn-in" and non-monotonic behavior, where the *y*-intercept and the slope are used to estimate/project the T80 duration.

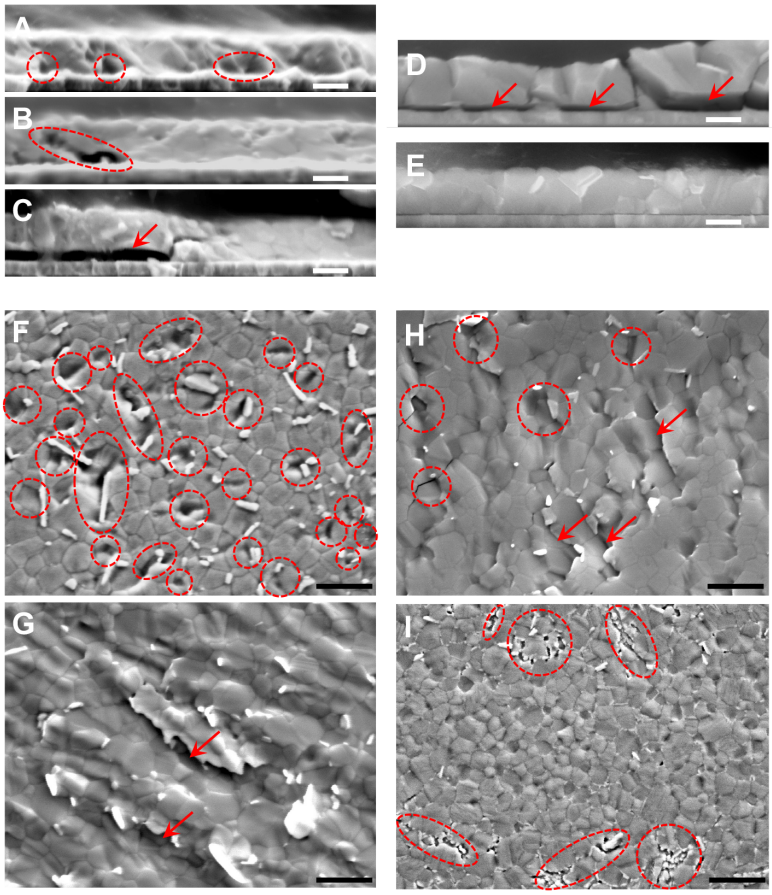

Figure 4. Characterization of operational-stability-tested PSCs. (A-C) Cross-sectional SEM images of the PSC without SAMs tested for 757 h showing morphological degradation at the ETL/MHP interface: (A) small voids (dashed circles/ovals), (B) large voids (dashed oval), and (C) delamination (arrow). (D) Cross-sectional SEM image of the PSC with H-SAM tested for 754 h showing delamination (arrows). (E) Cross-sectional SEM image of a PSC with I-SAM tested for 1,331 h with intact ETL/MHP interface. (F-G) SEM images of fracture surface (perovskite bottom side) of the PSC without SAMs showing: (F) small and large voids (dashed circles/ovals) and (G) interfacial delamination (arrows). (H) Corresponding SEM image of the PSC with H-SAM showing voids (dashed circles/ovals) and delamination (arrows). (I) Corresponding SEM image of the PSC with I-SAM showing minimal morphological degradation (dashed circles/ovals). Scale bars: (A-E) = 0.5 μm; (F-I) = 1 μm.

Table 1. PV performance parameters extracted from the *J-V* data, in reverse (R) and forward (F) scans, in Fig. 2E of "champion" PSCs without SAMs, and ones with H-SAM or I-SAM.

PSC	Scan	V_{OC} (V)	J_{SC} (mA.cm^{-2})	FF	PCE (%)
without SAMs	R	1.131	23.02	0.774	20.15
	F	1.117	22.99	0.721	18.52
with H-SAM	R	1.143	23.18	0.762	20.19
	F	1.142	22.86	0.760	19.84
with I-SAM	R	1.185	23.26	0.778	21.44
	F	1.182	23.22	0.759	20.83

Supplementary Materials:

Materials and Methods

Supplementary Text

Figures S1-S11

Tables S1-S4

Science
AAAS

Supplementary Materials for

Interfacial toughening with self-assembled monolayers enhances perovskite solar cell reliability

Zhenghong Dai, Srinivas K. Yadavalli, Min Chen, Ali Abbaspourtamijani, Yue Qi,

Nitin P. Padture

Correspondence to: nitin_padture@brown.edu

This PDF file includes:

Materials and Methods

Materials

All materials used in the experiments were obtained commercially and used without further purification, which include: N,N-dimethylformamide (DMF; 99.8%, Acros Organics, USA), dimethyl sulfoxide (DMSO; 99.7%, Acros Organics, USA), cesium iodide (CsI; 99.999%, Alfa-Aesar, USA), formamidinium iodide (FAI; Greatcell Solar, Australia), methylammonium bromide (MABr; Greatcell Solar, Australia), Pb(II) iodide (PbI_2; 99.99%, TCI), Pb(II) bromide ($PbBr_2$; >98%, Sigma-Aldrich, USA), chlorobenzene (CB; 99.8%, Sigma-Aldrich, USA), (3-iodopropyl)trimethoxysilane (>95%, Sigma-Aldrich, USA), (3-bromopropyl)trimethoxysilane (>97%, Sigma-Aldrich, USA), propyltrimethoxysilane(>98%, TCI, USA), isopropanol (IPA; 99.5%, Sigma-Aldrich, USA), Spiro-OMeTAD (Merck, Germany), bis(trifluoromethane)sulfonimide lithium salt (LiTFSI; 99.95%, Sigma-Aldrich, USA), Co(III) TFSI salt (FK 209; Greatcell Solar, Australia), acetonitrile (ACN; 99.9%, Acros Organics, USA), 4-tert-butylpyridine (t-BP; 96%, Sigma-Aldrich, USA), [6,6]-phenyl-C_{61}-butyric acid methyl ester (PCBM; 1-Material, Canada), tin oxide nanoparticles (SnO_2; 15 % in H_2O, Alfa-Aesar, USA), poly(methyl methacrylate) (PMMA; Sigma-Aldrich, USA), and epoxy adhesive (Hysol, USA).

Device Fabrication

Perovskite solar cells (PSCs) were fabricated with the following structure: glass/ ITO/SnO_2/SAM/MHP/Spiro-OMeTAD/Au, as shown schematically in Fig. 2A (ITO = indium-doped tin oxide; metal halide perovskite (MHP) = $Cs_{0.05}(FA_{0.85}MA_{0.15})_{0.95}Pb(I_{0.85}Br_{0.15})_3$ with 4 mol% excess PbI_2). The ITO-coated glass was pre-cleaned successively in ultrasonic baths of detergent solution, deionized water, ethanol, acetone, and isopropanol, for 15 min each, and further treated with UV-ozone for 30 min. A dilute SnO_2 nanoparticle solution (2.67 wt%) was spin-coated onto the substrates at 3,000 rpm for 30 s and annealed at 150 °C for 30 min to form a compact SnO_2 electron transport layer (ETL; ~30 nm thickness) (*33*). For PSCs with H-SAM or with I-SAM, the as-fabricated glass/ITO/SnO_2 substrates were submerged in a 5 mM solution of propyltrimethoxysilane ($Si(OCH_3)_3(CH_2)_3H$) or (3-iodopropyl)trimethoxysilane ($Si(OCH_3)_3(CH_2)_3I$), respectively, in isopropanol/DI water (v/v 95/5) for 1 h. Subsequently, the substrates were dried under flowing dry N_2 and annealed at 100 °C for 5 min, which were further rinsed with isopropanol several times before drying under N_2 again. For PSCs without SAMs, the substrates were treated with UV-ozone for 15 min.

MHP 1.4 M precursor solution was prepared by dissolving appropriate amounts of CsI, FAI, MABr, $PbBr_2$, and PbI_2 in DMF/DMSO (v/v 4/1) mixed solvent with 4 mol% excess PbI_2. The MHP layer (~500 nm thickness) was deposited by spin-coating the precursor solution at 6,000 rpm for 30 s. At the 20th second of spinning, 250 μL of anti-solvent chlorobenzene was dripped at the center. Subsequently, the as-deposited films were annealed at 110 °C for 50 min.

The Spiro-OMeTAD solution was prepared by dissolving 60 mg of Spiro-OMeTAD with additives in 700 μL of chlorobenzene. 15.5 μL of Li-TFSI solution (520 mg/ml in ACN), 12.5 μL of Co(III) TFSI salt (375 mg/ml in ACN), and 22.5 μL of t-BP were added to the solution. The Spiro-OMeTAD hole transport layer (HTL; ~300 nm thickness) was prepared by spin-coating the solution at 3,000 rpm for 30s. Both of MHP and HTL deposition were performed in a N_2-filled glovebox. Finally, 80-nm of Au layer was thermally-evaporated on top of the HTL as an electrode.

Electron-only transport devices (glass/FTO/SnO_2/MHP/PCBM/Ag) without SAMs, and ones with H-SAM or I-SAM at the SnO_2/MHP interface (FTO = fluorine-doped tin oxide), were fabricated for current (*I*) – voltage (*V*) measurements using above methods, where the PCBM was deposited by spin-coating the precursor solution (30 mg/mL in chlorobenzene) at 3,000 rpm for 30 s. A 100-nm of Ag layer was thermally-evaporated on top of the PCBM layer.

Mechanical Testing

The "sandwich" double-cantilever beam (DCB) specimens were prepared with the following structure: glass/ITO/SnO_2/SAM/MHP/PMMA/epoxy/ITO/glass. The dimension of the ITO-coated glass substrate used is 37.5×12.5×1 mm^3. The deposition of SnO_2, SAM, and MHP followed the afore-mentioned procedure. To study the effect of halogen terminal group, specimens with Br-SAM ((3-bromopropyl)trimethoxysilane ($Si(OCH_3)_3(CH_2)_3Br$) were also fabricated. The PMMA layer (~800 nm) was deposited onto MHP for protection by spin-coating the PMMA solution (8 wt% in CB) at 3000 rpm for 60 s. This was allowed to dry at room temperature for 1 h. Subsequently, a thin layer of epoxy (~2 μm) was applied onto the PMMA layer to "glue" another cleaned ITO-coated glass substrate on top. The PMMA layer was necessary to prevent any adverse reactions between the epoxy and the MHP layers. About 5-mm strip at the short edge was masked prior to epoxy application to create a "notch." The DCB specimens were then cured in a drybox

for 24 h, and the excess epoxy at the other edges was cleaned off carefully before mechanical testing was conducted.

The DCB specimens were tested using a method described elsewhere (*10, 12, 14, 16*). Briefly, a planar pre-crack was introduced along the width (B=12.5 mm) dimension of the specimen by inserting a razor blade into the "notch." Aluminum tabs were glued to the glass substrates on either side of the "sandwich" specimen at the cracked end of the long dimension (37.5 mm). Initially, a pre-load of 0.2 N was applied to ensure a good contact between the specimen and the instrument. The cracked DCB specimens were then loaded in tension with a displacement rate of 1 μm/s using a delaminator system (DTS, USA) until a well-defined planar crack at the MHP/SnO_2 interface was obtained. The load (P) - displacement (Δ) response was recorded at all times. The specimen was then partially unloaded, and reloaded where the crack length, a, was estimated using the compliance method, in conjunction with the following relation (*10*):

$$a = \left(\frac{d\Delta}{dP} * \frac{BEh^3}{8}\right)^{\frac{1}{3}} - 0.64h, \qquad \text{(S1)}$$

where B (=12.5 mm) and E (=70 GPa) are the width and the Young's modulus of the glass substrate, respectively, and h (=1 mm) is the half-thickness of the DCB specimen. The toughness, G_C, is then given by the relation (*10*):

$$G_C = \frac{12{P_C}^2 a^2}{B^2 E h^3}\left(1 + 0.64\frac{h}{a}\right)^2, \qquad \text{(S2)}$$

where P_C is the load at the onset of non-linearity in the P-Δ curve during the loading cycle. The loading-unloading cycles were repeated for four more times, and the G_C was calculated for the four cycles (excluding the initial "settling-in" loading cycle). The average G_C is reported for each such test. Examples of loading-unloading curved are presented in fig. S1. Ten to twelve DCB specimens were tested each for without SAMs, with H-SAM, with I-SAM, and with Br-SAM cases, where the G_C values, the averages, and the standard deviations are reported for each set. We note that the plasticity of the PMMA layer could contribute to the measured G_C. However, since the PMMA layer is very thin (~800 nm), that contribution is expected to be insignificant, and it does not affect the observed trends. Nevertheless, caution must be exercised in comparing the G_C values measured here with those measured by others using different specimen-architectures or methods.

The G_C of the DCB specimens after continuous exposure to 1-sun LED illumination (from the SnO_2 side) for 120 h and 240 h (in air; ~35 °C, ~40% RH) were also measured for (six specimens each): without SAMs, with H-SAM, and with I-SAM. The G_C values, the averages, and the standard deviations are reported for each set.

Characterization

A high-resolution scanning electron microscope (SEM; Quattro ESEM, ThermoFisher Scientific, USA) was used to observe top surfaces, fracture surfaces, and cross-sections of the samples. MHP grain sizes were determined using the linear-intercept method applied to the SEM images, in conjunction with the ImageJ image-analysis software, where 100-200 grains were used for each set of materials. The naturally formed grooves between grains were assumed to represent the grain boundaries, as such the estimated grain size is considered to be the "apparent" grain size.

X-ray diffraction (XRD) of top surfaces of MHP thin films was performed (Cu K_α radiation) using a high-resolution diffractometer (Discovery D8, Bruker, Germany).

X-ray photoelectron spectroscopy (XPS) of the SAMs-deposited surfaces was performed (K-Alpha, ThermoFisher, USA).

Device Testing

The *J-V* characteristics of PSCs were measured using a 2400 source meter (Keithley, USA) under simulated 1-sun illumination (AM1.5G, 100 $mW \cdot cm^{-2}$) which is generated by an Oriel Sol3A Class AAA solar simulator (Newport, USA) in air (RT, 40%-60% RH). The light intensity was calibrated using a standard Si photodiode. Typically, the measurements were performed in reverse (R) scan (from V_{OC} to J_{SC}) and forward (F) scan (from J_{SC} to V_{OC}) with a step size of 8 mV and a delay time of 10 ms. A typical active area of 0.105 cm^2 was defined using a non-reflective mask. All the PSCs were measured without any pre-conditioning. The hysteresis index (%) was determined using the relation $(PCE_R\text{-}PCE_F/PCE_F)\times100$. The maximum-power output stability of PSCs was measured by monitoring the stabilized current density output at the maximum-power-point (MPP) bias (deduced from the reverse scan *J-V* curves). External quantum efficiency (EQE) of the PSCs was measured using an internal quantum efficiency system (IQE-200B, Newport, USA) under the irradiation by a 100 W xenon lamp.

For continuous operational-stability test, unencapsulated PSCs were loaded in a sealed chamber with a transparent quartz cover under continuous 1-sun intensity white-LED illumination (Candlelight Systems, Switzerland). A continuous flow of dry N_2 was supplied to the chamber to minimize the water and oxygen content in the atmosphere (RT, RH<5%). The light intensity was monitored and maintained throughout the test. The PSCs were biased at the MPP voltage and the PCE was measured every hour with a MPP-tracking routine using a potentiostat with a standard perturb-and-observe algorithm (*44*). *J-V* characteristics were measured every 12 h.

The *J-V* characteristics of the PSCs before and at the end of the operational-stability tests were measured using the Keithley-Newport system above.

I-V measurements of the electron-only transport devices using the 2400 source meter (Keithley, USA) were performed in air, from 0 V to 1.2 V with a step size of 0.02 V and a delay time of 1 s. The trap-filled-limited voltages (V_{TFL}) were estimated by linear fitting of the *I-V* responses. The trap densities were estimated using the following relation:

$$n_{\mathrm{Trap}} = \frac{2\varepsilon_o\varepsilon_r V_{TFL}}{eL^2}, \qquad \text{(S3)}$$

where ε_o is the permittivity of free space, ε_r is the relative dielectric constant (~28), e is the elementary electron charge, and L is the thickness of the MHP layer (~500 nm).

DFT Modeling

All density functional theory (DFT) calculations were performed using Vienna *Ab initio* Simulation Package (VASP) (*35, 36*). GGA-PBE exchange-correlation functional was employed alongside Grimme D3 correction scheme for dispersion effects (*37, 38, 39*). The cutoff energy for the plane wave basis sets was chosen as 500 eV. 4×4×4 and 4×4×1 Γ-centered grids of k-points were used for bulk and slab calculations, respectively. All the geometry optimizations were done with no constraints until the residual of forces became smaller than 0.0001 $eV.Å^{-1}$. The cubic α-$FAPbI_3$ (001) plane was chosen based on its stability (*40, 41*). Two different surface terminations were chosen, namely, PbI_2- and I-terminated structures to probe the nature of the bonding. An 1×1

simulation cell (6.36×6.36 $Å^2$ based on the relaxed bulk structure) with either 7 (PbI_2-terminated) or 8 (I-terminated) atomic layers along with at least 25-Å thick vacuum layer normal to the (001) plane constitute the slab model. In order to maintain computational tractability, aligned H-terminated butane ($H(CH_2)_4H$) and I-terminated butane (($H(CH_2)_4I$) molecules were used as proxies for H-SAM and I-SAM, respectively. In addition, similar interfaces with F-terminated butane (($H(CH_2)_4F$) was also studied ("F-SAM"). The "SAM" slab contained either one molecule per cell (fig, S6A (left; side-view) or two molecules per cell (fig. S6A (right; top-view)). The interface was formed by bringing the "SAM" molecule with either H, I or F pointing toward the α-$FAPbI_3$(001) surface, at an initial separation of r~3 Å followed by full geometry optimizations. The bond-distance after optimization is reported in Table S2. The adhesion property was measured by the work of separation, W_{sep} (*42*), defined as the energy difference between the fully-optimized interface, E_i^{DFT}, and the unoptimized separated (r~8 Å in fig. S6A) interface structures ($E_{r=8}^{DFT}$), divided by the interface area, A:

$$W_{sep} = \frac{1}{A}(E_i^{DFT} - E_{r=8}^{DFT}). \quad \text{(S4)}$$

The computed W_{sep} for different interfaces are listed in Table S2. The charge density difference for the interface structure before and after the bond formation was plotted to reveal the nature of the bonding.

Supplementary Text

DFT Modeling

The computed W_{sep} and the bond-distance in the optimized interface structure are listed in Table S2. The charge-transfer-density difference plots shown in fig. S6, and in Fig. 1C, and Fig. 1D in the main text, illustrate the nature of the bonding at the interface between $H(CH_2)_4H$ ("H-SAM") or $H(CH_2)_4I$ ("I-SAM"), and different α-$FAPbI_3$ (001) MHP surface terminations. The I-atom on the "I-SAM" has an electrophilic region to attract electrons. Since I on the I-terminated surface is undercoordinated (noted as $I^{0.5-}$ according to formal charge balance) and I on the PbI_2-terminated surface is fully coordinated (noted as I^-), the I..."I-SAM" bond length is shorter and the bond stronger with the fully-coordinated I^-, which is nucleophilic. The undercoordinated Pb (noted as $Pb^{1.67+}$) on the PbI_2 surface also has electrons to donate and it forms the shortest bond with "I-SAM." Therefore, the PbI_2-terminated α-$FAPbI_3$ interfacing two "I-SAM" per cell has the strongest interfacial bonding and $W_{sep.}$ In comparison, the W_{sep} with "I-SAM" is always higher than that with "H-SAM," due to more electron transfer toward "I-SAM." Furthermore, there does not appear to be a direct chemical bond between "H-SAM" and any of the α-$FAPbI_3$ surface terminations examined in this work. For instance, in the case of "H-SAM" interacting with an I-terminated surface, no evidence of significant charge transfer is observed (fig. S6B (left)). The same can be deduced in the case of "H-SAM" interaction with PbI_2-terminated α-$FAPbI_3$ surfaces for both one and two SAMs coverages (fig. S6C (left) and Fig. 1C). Moreover, the H…Pb distance in the case of "H-SAM" on PbI_2-terminated surface is 2.95 Å. This value is much longer than the typical Pb-H bonding distance of 1.73 Å, as measured for PbH_4 molecule. This is another piece of evidence which indicates that there is no direct bonding between "H-SAM" and PbI_2-terminated α-$FAPbI_3$ surfaces. In the case of "I-SAM" interfaced with I-terminated and PbI_2-terminated α-$FAPbI_3$ surfaces, both electron gain (yellow) and electron loss (blue) regions are identifiable (Fig. 1D, fig. S6B (right), and fig. S6C (right)), leading to the conclusion that at least partial bonding

exists as a result of attractive electrostatic interactions between the two regions. This type of bonding has the characteristics of the halogen bond (*43*), and it is more pronounced in the case of "I-SAM" interfaced with PbI_2-terminated α-$FAPbI_3$ surface.

To further investigate the nature of bonding between SAMs and the MHP surfaces, we also performed computational control experiments using "F-SAM" as the probe molecule. The results indicate a weaker SAM-surface interaction for "F-SAM" as compared to "I-SAM". All the computed values of W_{sep} for "F-SAM" are smaller than their "I-SAM" counterparts (Table S2). If the interaction between the SAM and the surface was predominantly of electrostatic nature, the larger electronegativity difference between the F on "F-SAM" and surface Pb as compared to the I on "I-SAM" and surface Pb would lead to a higher W_{sep} for "F-SAM" as compared to "I-SAM." This indicated that halogen bonding, the strength of which decreases with the electrophilic order: I > Br > Cl > F, plays a key role in the interaction between the MHP surface and the SAMs proxy molecules.

While the DFT-calculated absolute W_{sep} values in Table S2 are quite small compared to the measured G_C values in Table S1, it is more instructive to consider the relative contributions of the "H-SAM" and "I-SAM" towards the overall adhesion. Also, the DFT calculations now provide a better understanding of the nature of the bonding between SAMs and MHP surfaces.

PSCs Operational-Stability Tests

The method for estimating/extrapolating T80 duration of a PSC is described by Khenkin, *et al*. (*44*), where the steady-state PCE degradation part of the data is fitted to a line. The *y*-intercept provides the "new" normalized PCE of 1.0. Using this as the reference, time at normalized PCE of 0.8 is the estimated (intrapolated) T80 for PSCs without SAMs and with H-SAM. For extrapolation of T80 for the PSCs with I-SAM, the same procedure is used, except the slope of the linear fit is used to extrapolate to T80. The linear-regression fits to the five operational-stability-tested PSCs in Fig. 3 are:

without SAMs:	$y = -2.60\times10^{-4}x + 0.8997$	T80 ~692 h
with H-SAM	$y = -2.85\times10^{-4}x + 1.0180$	T80 ~714 h
with I-SAM-1:	$y = -6.39\times10^{-5}x + 0.9605$	T80 ~3,006 h
with I-SAM-2:	$y = -1.02\times10^{-4}x + 0.9671$	T80 ~1,896 h
with I-SAM-3:	$y = -4.64\times10^{-5}x + 0.9096$	T80 ~3,921 h

Supplementary Figures

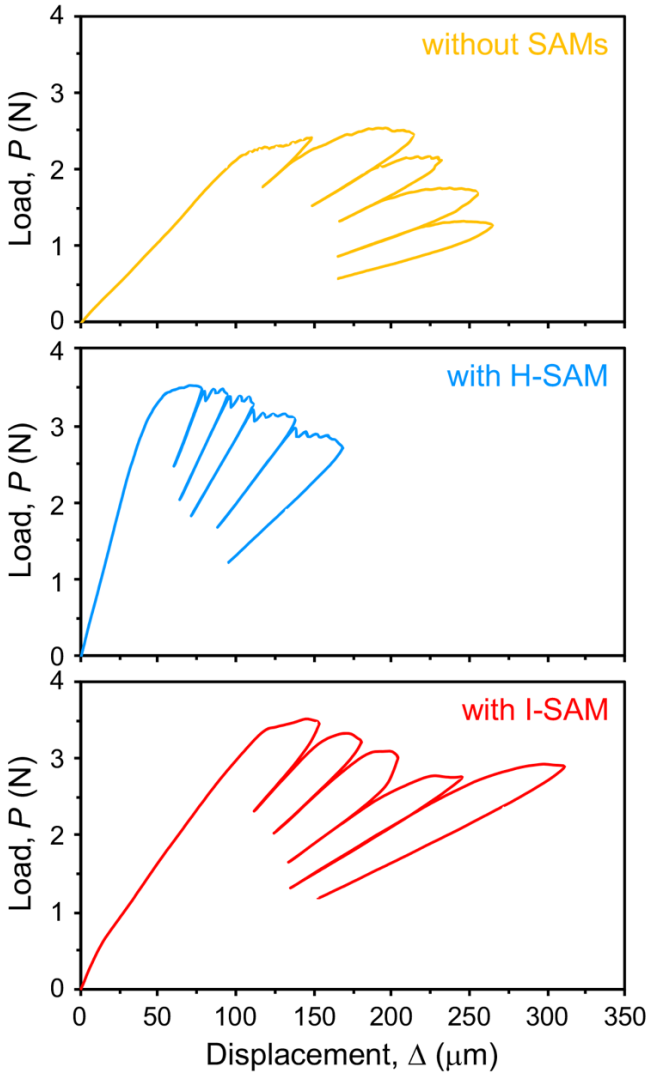

Fig. S1. Representative P-Δ loading-unloading curves for the measurement of G_C of the "sandwich" DCB specimens: (A) without SAMs, (B) with H-SAM, and (C) with I-SAM.

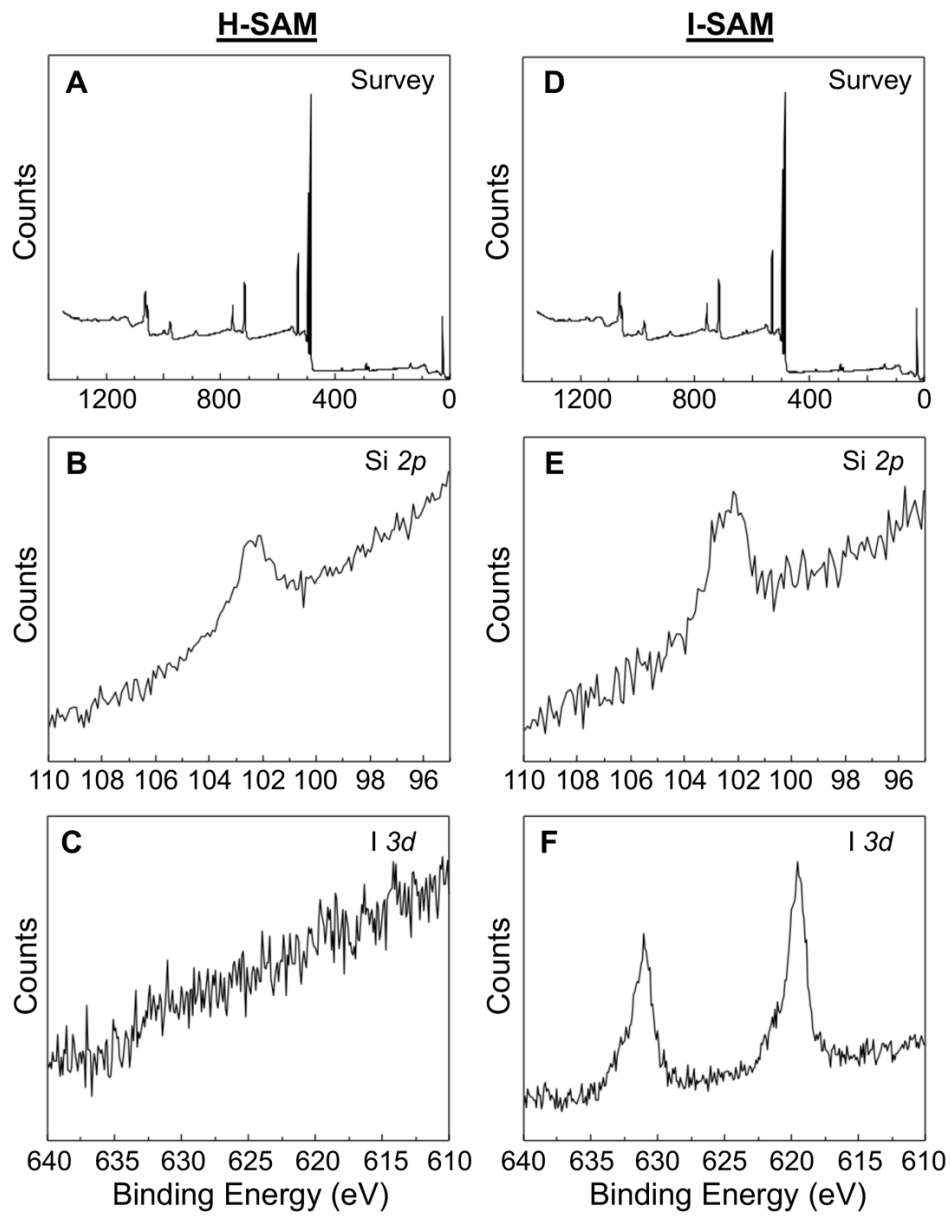

Fig. S2. XPS spectra from top-surface of SnO_2 ETL with SAMs deposited: (A) survey (with H-SAM), (B) Si 2*p* core level (with H-SAM), (C) I 3*d* core level (with H-SAM), (D) survey (with I-SAM), (E) Si 2*p* core level (with I-SAM), and (F) I 3*d* core level (with I-SAM).

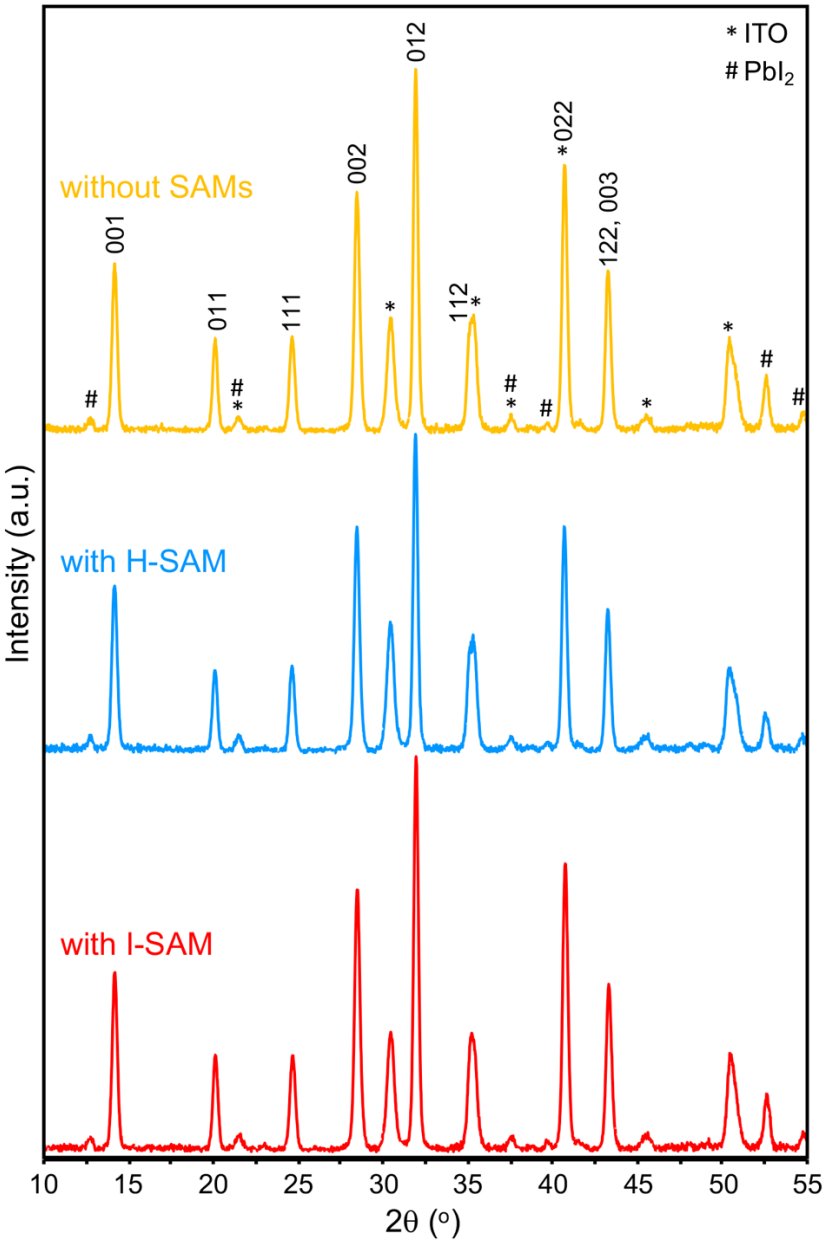

Fig. S3. Indexed XRD patterns from top-surfaces of the MHP thin films deposited on SnO_2 ETL without SAMs, with H-SAM, and with I-SAM. ITO substrate (*) and PbI_2 (#) peaks are marked.

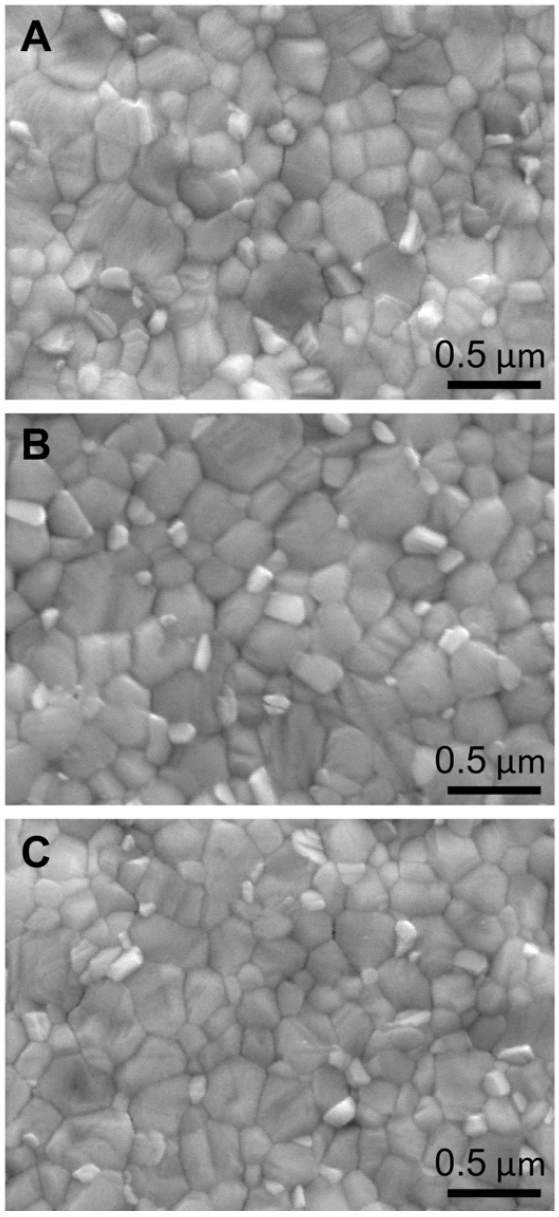

Fig. S4. Top-surface SEM micrographs of MHP thin films deposited on SnO_2 ETL: (A) without SAMs, (B) with H-SAM, and (C) with I-SAM underneath.

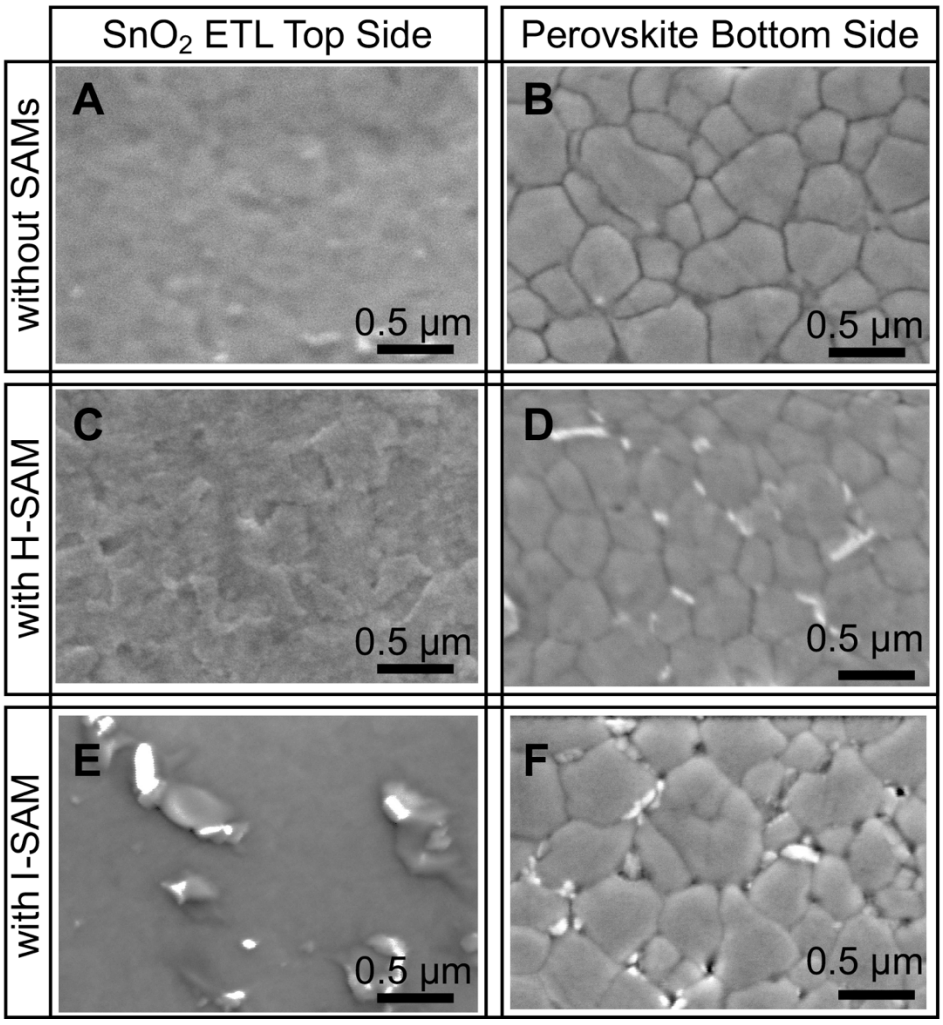

Fig. S5. SEM images of delaminated fracture surfaces: (A) without SAMs (SnO_2 ETL top side), (B) without SAMs (perovskite bottom side); (C) with H-SAM (SnO_2 ETL top side), (D) with H-SAM (perovskite bottom side); and (E) with I-SAM (SnO_2 ETL top side), and (F) with I-SAM (perovskite bottom side).

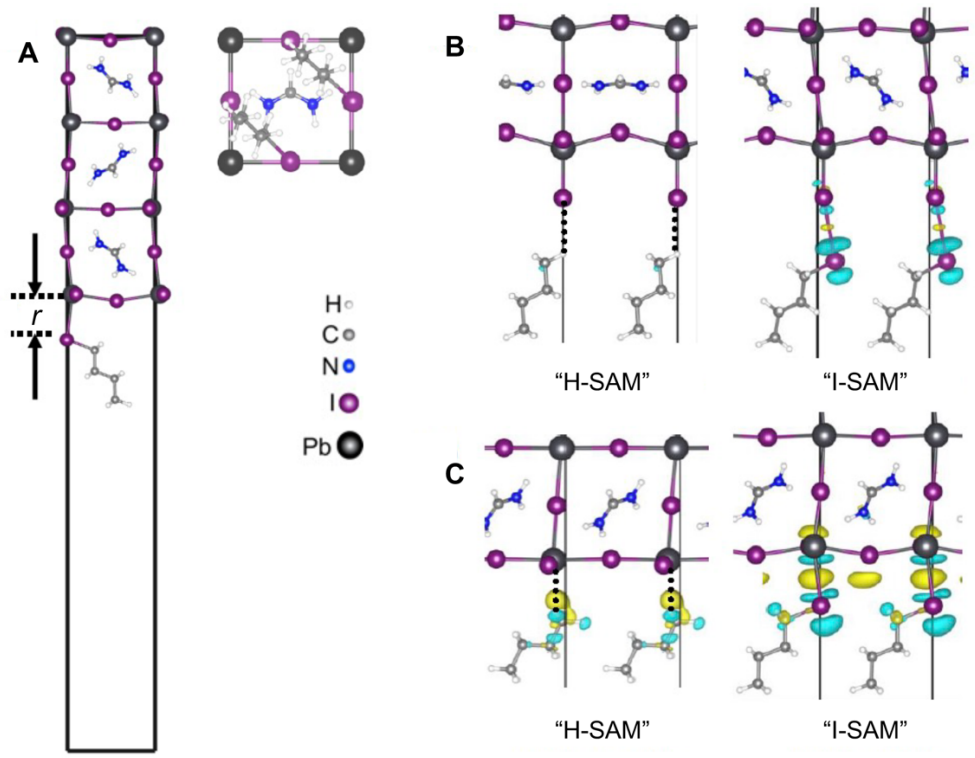

Fig. S6. (A) Schematic illustrations of the simulation cell of "I-SAM"/α-$FAPbI_3$ interface, where *r* refers to the interface separation. The side view (left) shows the PbI_2–terminated α-$FAPbI_3$ interfacing with one "I-SAM" molecule per cell, and the top-view (right) shows the PbI_2-terminated α-$FAPbI_3$ interfacing with two "I-SAM" molecules per cell. (B) Charge-transfer density difference plots for $H(CH_2)_4H$ ("H-SAM") (left) and $H(CH_2)_4I$ ("I-SAM") (right) interfaced with I-terminated α-$FAPbI_3$ (001) surface (one molecule/cell). (C) Charge-transfer-density difference plots for "H-SAM" (left) and "I-SAM" (right) interfaced to Pb on the PbI_2-terminated α-$FAPbI_3$ (001) surface (one molecule/cell). The yellow or blue color indicates electron gain or loss above 0.0007 $e.Å^{-3}$, respectively. Dashed lines across the interface indicate no bonding.

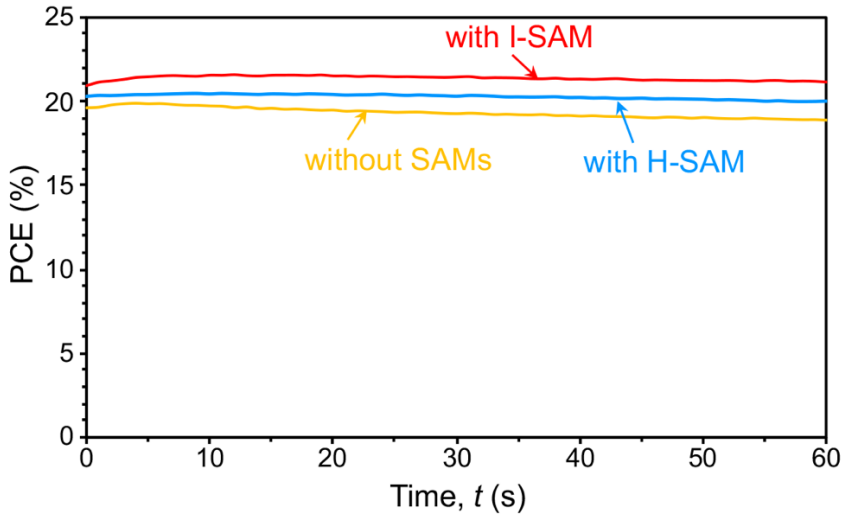

Fig. S7. Stabilized PCE outputs at MPP of "champion" PSCs: without SAMs (0.95 V bias), with H-SAM (0.95 V bias), and with I-SAM (1.0 V bias).

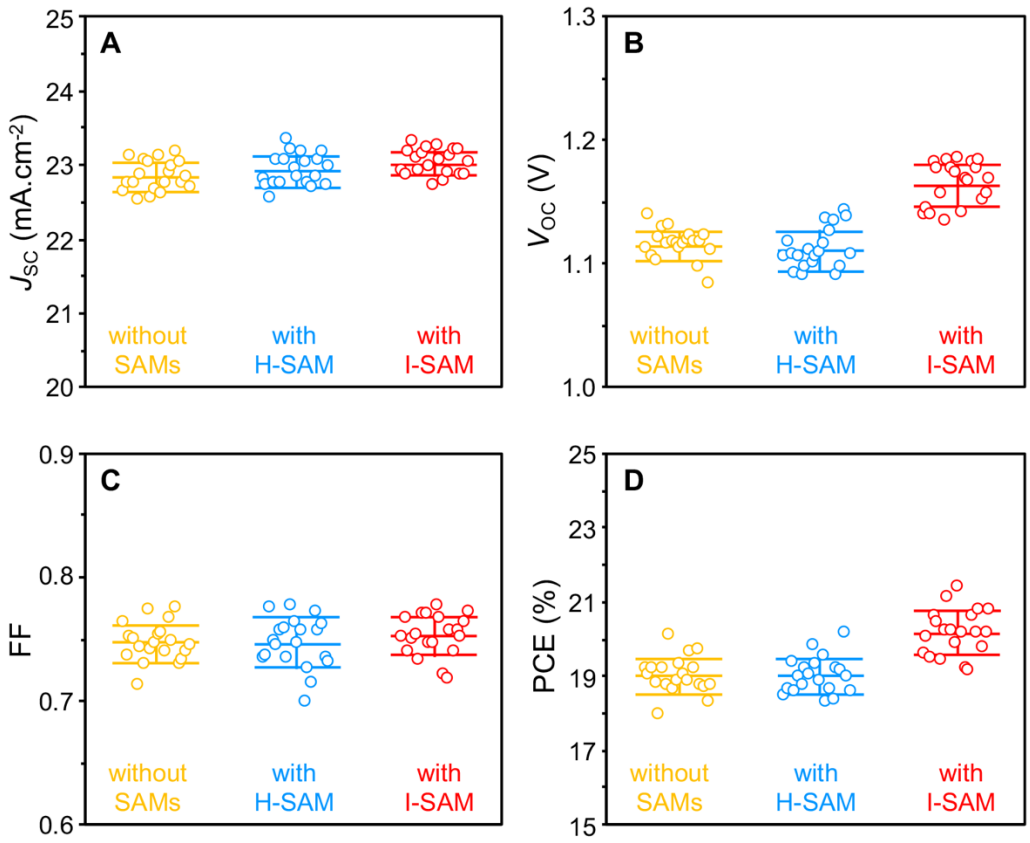

Fig. S8. PV performance parameters from *J-V* characteristics measured in reverse (R) scan of 20 each PSCs without SAMs, with H-SAM, and with I-SAM: (A) J_{SC}, (B) V_{OC}, (C) FF, and (D) PCE. Average ± standard deviation indicated.

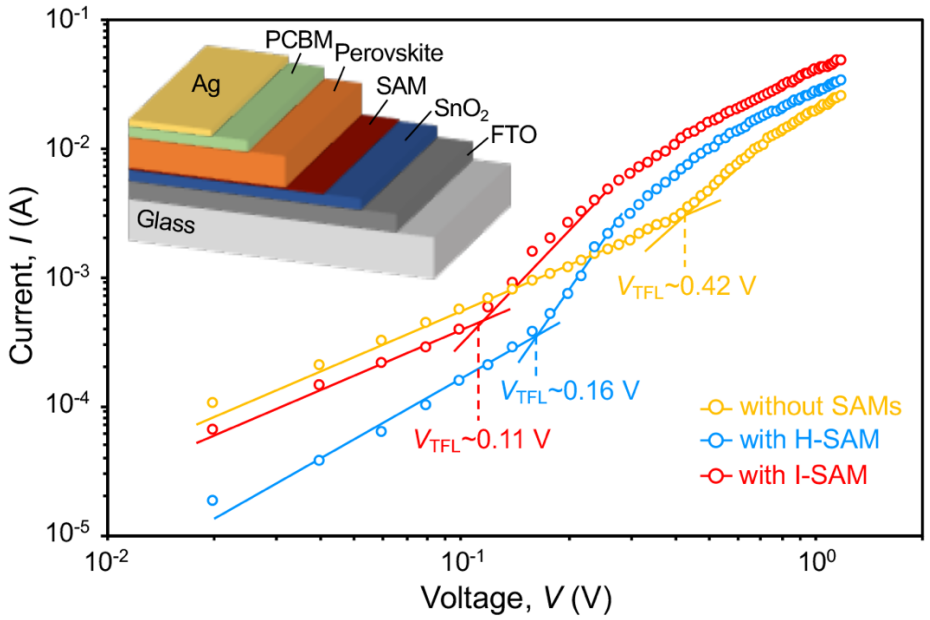

Fig. S9. *I-V* responses from electron-only transport devices (inset: schematic (not to scale)) without SAMs, with H-SAM, and with I-SAM, where the V_{TFL} values are estimated at 0.42 V, 0.16 V, and 0.11 V, respectively. These values are used to estimate the trap densities (n_{Trap}) using Eqn. S3.

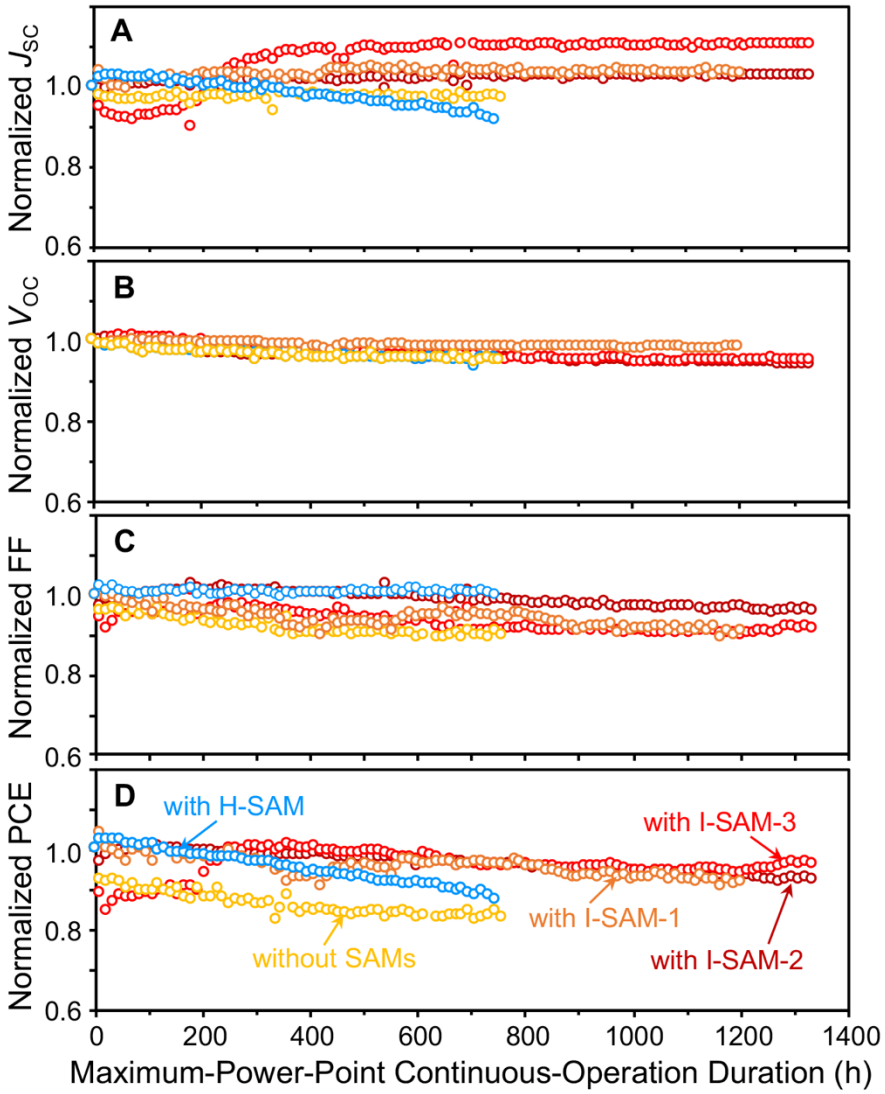

Fig. S10. Normalized PV parameters from *J-V* responses (recorded approximately every 12 h) as a function of time during operational-stability testing of PSCs without SAMs, with H-SAM, and with I-SAM (three devices): (A) J_{SC}, (B) V_{OC}, (C) FF, and (D) PCE. Operational-stability testing conditions: 1-sun continuous illumination, MPP-tracking, unencapsulated, flowing N_2 atmosphere, and room temperature. Note that PCE from the *J-V* response is typically higher than that measured during MPP tracking (*44, 45*).

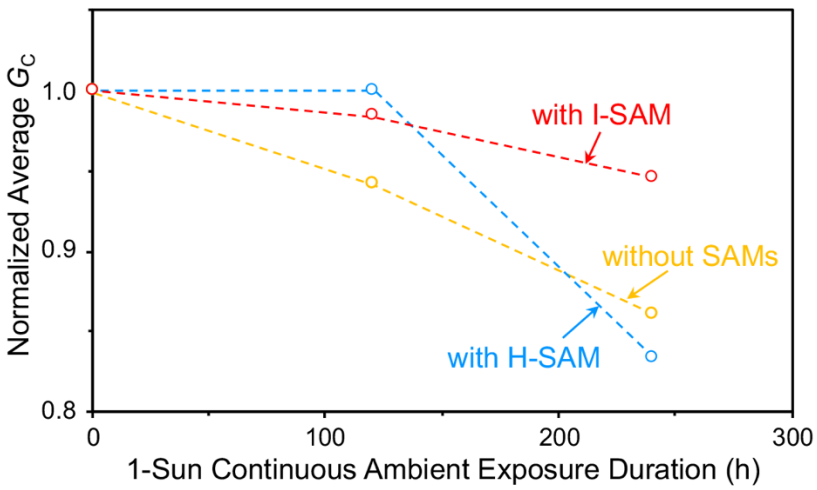

Fig. S11. Normalized average G_C as a function of continuous exposure to 1-sun (LED) before testing of "sandwich" DCB specimens (six each): without SAMs, with H-SAM, and with I-SAM. See table S4 for G_C values.

Supplementary Tables

Table S1. Interfacial toughness (G_C) values of 10-12 specimens/tests each of ETL/MHP interface without SAMs, with H-SAM, with I-SAM, and with Br-SAM measured using the DCB delamination method (Fig. 1A).

#	without SAMs G_C (J.m^{-2})	with H-SAM G_C (J.m^{-2})	with I-SAM G_C (J.m^{-2})	with Br-SAM G_C (J.m^{-2})
1	1.11	0.85	2.27	1.65
2	1.32	1.07	2.36	1.79
3	1.37	1.17	2.55	1.81
4	1.48	1.42	2.61	1.90
5	1.66	1.49	2.65	1.98
6	1.95	1.75	2.72	2.02
7	2.09	1.82	2.79	2.26
8	2.19	1.82	3.09	2.32
9	2.32	1.91	3.11	2.36
10	2.41	2.21	3.12	2.66
11	2.44	2.37	3.33	-
12	2.58	2.79	3.34	-
Avg. ±SD	1.91 ±0.48	1.72 ±0.54	2.83 ±0.35	2.08 ±0.31

Table S2. DFT results for W_{sep} for "SAM" on different surface terminations of α-$FAPbI_3$ (001). Here, "—" indicates bond formation with charge transfer, and "…" indicates no chemical bond formation.

Termination/ #-"SAM" per Cell	"H-SAM"		"I-SAM"		"F-SAM"	
	W_{sep} ($J.m^{-2}$)	Bond Type (Length Å)	W_{sep} ($J.m^{-2}$)	Bond Type (Length Å)	W_{sep} ($J.m^{-2}$)	Bond Type (Length Å)
I/One-"SAM"	0.027	H…I (3.17)	0.072	I—I (3.74)	0.016	F…I (3.26)
PbI_2/One-"SAM"	0.092	H…Pb (2.95)	0.190	I—Pb (3.38)	0.074	F—Pb (2.82)
PbI_2/Two-"SAM"	0.103	H…Pb (3.22) H…I (3.69)	0.254	I—Pb (3.74) I—I (3.58)	0.172	F—Pb (2.80) F…I (5.19)

Table S3. Initial 'before' PV parameters of the all the operational-stability-tested PSCs, and PV parameters of the PSCs with H-SAM and with I-SAM (three devices) at the end of operational-stability tests ('after'), derived from the *J-V* responses measured using the Keithley-Newport testing system.

PSC	Duration (h)	J_{SC} (mA.cm^{-2})	V_{OC} (V)	FF	PCE (%)
without SAMs*	0	23.11	1.089	0.759	19.10
with H-SAM	0	23.07	1.105	0.746	19.02
	754**	22.66	1.056	0.708	16.94
with I-SAM-1	0	22.96	1.162	0.768	20.49
	1210**	23.05	1.130	0.704	18.34
with I-SAM-2	0	23.34	1.113	0.776	20.16
	1331**	23.24	1.079	0.752	18.86
with I-SAM-3	0	23.21	1.107	0.770	19.78
	1331**	23.07	1.084	0.730	18.26

* The PV parameters of the control PSC could not be removed from the Candlelight testing system after operational-stability testing for 757 h, therefore, its 'after' PV parameters could not be determined using the Keithley-Newport testing system.

** The operational-stability-tested PSCs rested in dark in a glovebox prior to the measurement of the 'after' PV parameters.

Table S4. Interfacial toughness (G_C) values of 6 specimens each of ETL/MHP interface without SAMs, with H-SAM, and with I-SAM measured using the DCB delamination method (Fig. 1A), subjected to continuous exposure to 1-sun white LED for 120 h or 240 h in the ambient (~35 °C, ~40% RH).

#	without SAMs G_C (J.m^{-2})		with H-SAM G_C (J.m^{-2})		with I-SAM G_C (J.m^{-2})	
	120 h	240 h	120 h	240 h	120 h	240 h
1	1.77	1.88	1.98	1.35	3.07	3.06
2	1.52	2.07	1.56	1.43	3.11	2.69
3	2.07	1.37	1.64	1.87	2.46	2.76
4	2.28	1.50	2.24	1.46	3.02	2.08
5	1.54	1.72	1.94	0.62	2.78	2.99
6	1.61	1.33	0.98	1.89	2.26	2.48
Avg. ±SD	1.80 ±0.28	1.65 ±0.27	1.72 ±0.40	1.44 ±0.42	2.78 ±0.32	2.68 ±0.33